Theoretical Limits of the Matching Bandwidth and Output Power of AlScN-Based HEMTs

Philipp Döring, Sebastian Krause, *Member, IEEE*, Christian Friesicke, and Rüdiger Quay, *Senior Member, IEEE*

***Abstract*—In this work, the simultaneously achievable matching bandwidth and output power of AlScN-based high electron mobility transistors (HEMTs) are derived and compared to conventional AlGaN, GaAs, and Si devices. Moll's method is used to extract time delays resulting in carrier velocities close to 1 × 10^7 cm/s for sheet carrier densities ≥ 1.5 × 10^{13} cm^{-2}. Subsequently, theoretical current densities of 2.5–4 A/mm and a maximum transconductance higher than 600 mS/mm are derived for low barrier thicknesses of 5–10 nm and Sc-concentrations of 5%–20%. The matching bandwidth is estimated by the Bode–Fano criterion and connected to the output power of the transistor by the power-bandwidth product, which accounts for both parameters simultaneously. AlScN-based devices are found to exhibit a 4.5-times higher power-bandwidth product compared to conventional AlGaN-based HEMTs, quantifying the enormous, theoretical limits. Experimental data already show an improvement by a factor of 1.45 for AlScN-based devices, even in this early stage of development, which proves their superior properties, when aiming for wideband high-power millimeter-wave (mm-wave) devices.**

***Index Terms*—AlScN, Bode–Fano limit, high-electron mobility transistor (HEMT), ScAlN.**

I. INTRODUCTION

AlScN/GaN heterostructures have drawn enormous attention for power, memory, and RF-applications due to their large polarization gradient [1] at the heterointerface and their ferroelectric properties [2]. Millimeter-wave (mm-wave) transistors are expected to provide a highly attractive trade-off in terms of aspect ratio (gate length/barrier thickness) with high-*k* dielectric properties [3] of the barrier material and high sheet carrier densities when compared to metal-polar or nitrogen-polar AlGaN/GaN-, AlN/GaN-, or InAlN/GaN-based devices [1]. Theoretical calculations of the elastic/dielectric properties [4] and electron accumulation [1], [5] of AlScN-based thin films and heterostructures were comprehensively described. However, theoretical predictions of the corresponding device performance and the benefits over common AlGaN-based high electron mobility transistors (HEMTs) have not been reported yet due to the lack of required material/transistor data.

This work provides an estimation of the intrinsic potential of AlScN/GaN HEMTs in terms of current density, transconductance, output power, and bandwidth. Theoretical data are compared with reported data in the literature and experimental data on fabricated AlScN/GaN HEMTs with 0.15 μm gate length. Moll's method is used to extract time delays experimentally, and corresponding high-field transport properties are reported for the first time. Even though the carrier velocity is slightly reduced, the high-*k* properties of AlScN are shown to allow for higher transconductance values in comparison to AlGaN/GaN HEMTs with the same barrier thickness. Based on the carrier velocity and current density of the intrinsic transistor the Bode–Fano limit with respect to the carrier density is derived, allowing for a quantitative estimation of the simultaneously achievable matching bandwidth and output power density of the transistors (power-bandwidth product). Theoretical data revealed a 4.5-times increase in power-bandwidth product compared to conventional AlGaN/GaN HEMTs. A 1.45-times increase in power-bandwidth product is achieved when using fabricated AlScN-based devices demonstrating an enormous improvement compared to classical heterostructures. In addition, the transition frequency is considered simultaneously by linking it to the power-bandwidth product. The results reveal the superior properties of AlScN HEMTs for future high-power mm-wave applications when aiming for large output power and matching bandwidth simultaneously.

II. EXPERIMENTAL SECTION

The fabrication of the devices in this work started with the epitaxial growth by metalorganic chemical vapor deposition of a Fe-doped buffer and an u.i.d.-GaN channel on 100 mm semi-insulating SiC substrates. Several heterostructures were

---

Manuscript received 26 September 2023; revised 3 November 2023 and 10 November 2023; accepted 14 November 2023. This work was supported in part by the German Federal Ministry of Defense, BMVg, and Federal Office of Bundeswehr Equipment, Information Technology and In-Service Support BAAINBw; in part by the German Federal Ministry of Education and Research (BMBF) within the Project EdgeLimit-Green ICT; and in part by the Fraunhofer Internal Programs SCALING. The review of this article was arranged by Editor G. I. Ng. *(Philipp Döring and Sebastian Krause contributed equally to this work.) (Corresponding author: Philipp Döring.)*

The authors are with the Fraunhofer Institute for Applied Solid State Physics (Fraunhofer IAF), 79108 Freiburg im Breisgau, Germany (e-mail: philipp.doering@iaf.fraunhofer.de; sebastian.krause@iaf.fraunhofer.de).

Color versions of one or more figures in this article are available at https://doi.org/10.1109/TED.2023.3334224.

Digital Object Identifier 10.1109/TED.2023.3334224

realized with AlN, AlScN, and AlGaN barriers with different thicknesses for AlGaN and AlScN to achieve different sheet carrier densities [6], [7], [8]. After the deposition of a Si-rich SiN$_x$ film, the 0.15-μm gate openings are defined by e-beam lithography before optically defining the dimensions of the gate head with an integrated gate field plate. Schottky-gate metallization is then evaporated, followed by gate-head passivation and formation of the source field plates. The gate-to-source and gate-to-drain distances are 0.7 and 1.2 μm, respectively [9], [10]. Hall structures were realized to measure the sheet carrier density on passivated and isolated fields. Additional transistors with a gate length of 0.25 and 0.5 μm are processed to extract the gate transit delay. Transistors with a gate width of $W_G = 2 \times 25$ μm were used to determine the saturation current and transconductance of the fabricated devices experimentally. A detailed description of the fabrication, small/large signal, transfer, and OFF-state characteristics can be found in [9] and [10].

III. DRAIN CURRENT VERSUS SHEET CARRIER DENSITY

The theoretical maximum current density of a HEMT can be estimated by the following equation:

$$I_{\mathrm{D,sat}} = q \times n_s \times \upsilon_{\mathrm{EFF}}(E, n_S) \tag{1}$$

where q, n_s, and υ_{EFF} are elementary charge, sheet carrier density, and effective carrier velocity, respectively. Two assumptions are made for this theoretical consideration: 1) extrinsic parameters, e.g., resistive losses are neglected; and 2) the effective carrier velocity is assumed instead of the saturation velocity. To estimate the potential drain current density for a given gate width of a specific material combination, the available sheet carrier density and the corresponding saturation or effective carrier velocity need to be known.

A. Sheet Carrier Density

The sheet carrier density in dependence of the barrier thickness can be estimated by electrostatic theory for III-N heterostructures [1], [11]. Up to five-times larger values of n_s were predicted for AlScN-based devices in previous reports [1], [12] when compared to common AlGaN-based devices. The sheet carrier density of a heterostructure is commonly derived by Hall measurements experimentally. Several data have been reported for n_s (unpassivated [6], [8], [13], [14] or passivated and isolated structures [9], [15], [16]) exceeding theoretical limits of AlGaN-based heterostructures even with aggressive Al content up to 40% (Fig. 1) or InAlN-based heterostructures [1]. However, the effective/saturation velocity of electrons in the 2DEG of III-nitride heterostructures under high fields is inversely proportional to n_s [17], [18]. Thus, the increase in carrier density will not be equivalent to the increase in current density of the final device.

B. Carrier Velocity

The carrier velocity under high electric fields, which is of major importance for power amplifiers, has not yet been systematically reported for AlScN-based HEMTs or high carrier densities $n_s > 2 \times 10^{13}$ cm^{-2}. To estimate the resulting

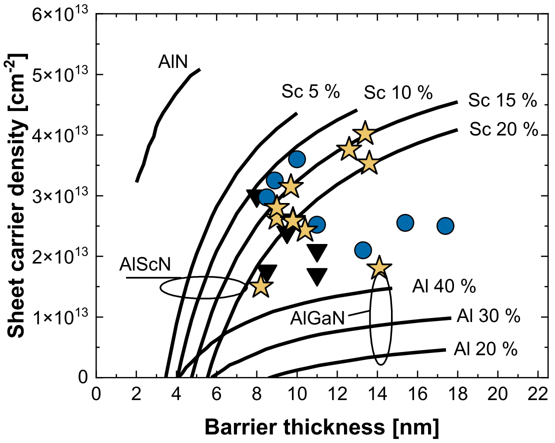

Fig. 1. Sheet carrier density versus barrier thickness limits for Al$_X$Ga$_{1-X}$N/GaN (x = 0.2–0.4), Al$_{1-X}$Sc$_X$N/GaN (0.05–0.2) and AlN/GaN heterostructures. Reported data are given in blue cubes (unpassivated [6], [7], [8], [9], [10], gray diamonds (passivated and isolated [14], [15], [16]) yellow stars (passivated and isolated, this work).

current density either the saturation velocity or the effective carrier velocity under the gate can be used. Measuring υ_{SAT} requires specific measurement structures to ensure the voltage drop in the related constrictions [17], [19]. In this, case the electric field can be estimated and the saturation velocity in dependence of the electric field can be derived. However, the electric field distribution in a transistor is different and dependent on the device geometry which affects the actual carrier velocity. Deriving the effective carrier velocity below the gate is closer to operation conditions but is superimposed by the transit time of the electrons from source to gate and gate to drain. A delay extraction is required to account for all contributors to the electron transit from source to drain. A suitable methodology to derive the channel charging delay was given by Moll et al. [20]. Reported data on υ_{SAT} and υ_{EFF} in dependence of n_s are given in Fig. 2 for different GaN-based heterostructures. However, only few data are reported aside from AlGaN/GaN-heterostructures. Stimulated longitudinal optical phonon emission (LOPE) was predicted to cause clamping of the electron velocity for high n_s with strong electron-phonon interaction and high phonon lifetime in GaN [17], [18]. Velocity saturation curves were modeled by the following equation:

$$\upsilon_{\mathrm{SAT}} = \frac{10^7}{0.38 + \left(\frac{n_S}{n_{S,0}}\right)^{0.45}}. \tag{2}$$

The model is in good agreement up to carrier densities of $n_s \leq 1 \times 10^{13}$ cm^{-2} for Ga- and N-Polar AlGaN-based devices [17], [21] but verification for higher n_s has not been given up to this point. Higher impact of scattering as well as carriers within the barrier could be expected for very large n_s as a result of the 2DEG centroid closer to the ternary barrier [5]. In addition, inter-subband distortion could be present for $n_s \geq 2 \times 10^{13}$ cm^{-2} [5], [22]. However, scattering mechanisms of ternary barrier materials with extremely high sheet carrier densities beyond $n_s > 3 \times 10^{13}$ cm^{-2} have not been systematically reported yet. In addition, subband

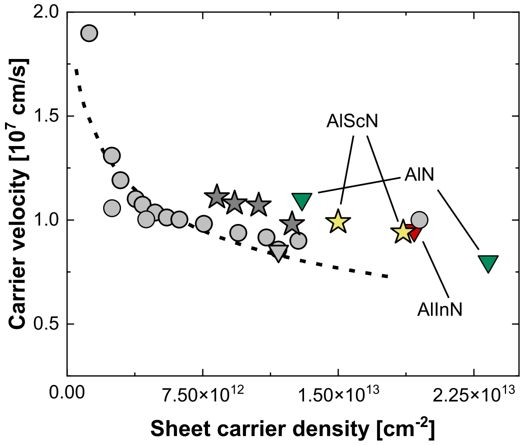

Fig. 2. Reported data on saturation velocity (circles) and effective carrier velocity from Moll's method (diamonds) [17], [22], [23], [24], [25]. Results of this work are given by stars for AlGaN/GaN (gray) and AlScN/GaN (yellow). The dashed line represents a fit to the LOPE-model described by (2).

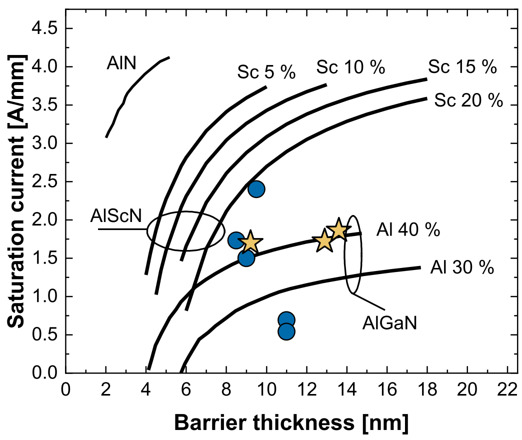

Fig. 3. Calculated maximum current density versus barrier thickness for Al$_x$Ga$_{1-x}$N/GaN ($x = 0.3\%$–0.4%), Al$_{1-x}$Sc$_x$N/GaN (0.05%–0.2%) and AlN/GaN heterostructures Reported data of devices from literature (blue circles [2], [14], [15], [16], [27]) and this work (yellow stars) are given additionally.

occupation has not been studied so far for AlScN devices. The effective carrier velocity for several devices with AlGaN and AlScN was derived by Moll's method for drain biases of $V_{\mathrm{DS}} = 5$, 10, and 15 V with negligible differences in delay times for all devices. The extracted data are given in Fig. 2 with the described LOPE model [17] and reported data on carrier velocities from other groups [17], [23], [24], [25], [26]. For AlScN-based devices a $\upsilon_{\mathrm{EFF}} = 0.99$ and 0.94×10^7 cm^2/s was derived for $n_s = 1.5$ and 1.86×10^{13} cm^{-2}, respectively. The extracted velocity of the AlScN-based device seems consistent with the LOPE model proposed for AlGaN. Slightly higher saturation velocities are observed for all data reported from Moll's method when compared to the LOPE model. The difference could be related to slight velocity overshoot [23] or different e-field strength at transistor operation as a result of, e.g., gate shape and gate length.

C. Saturation Current

Based on the theoretical sheet carrier densities and the extrapolated LOPE model, the maximum drain current densities of AlScN-based HEMTs can be estimated. It should be noted that υ_{EFF} is underestimated based on the experimentally obtained results described in Fig. 2. A comparison of the obtained $I_{\mathrm{D,sat}}$ versus t_{BAR} with reported data is given in Fig. 3. It is apparent that AlScN-based devices exhibit much larger theoretical drain current densities for a given barrier thickness than common AlGaN-based heterostructures. This holds especially true for barrier thicknesses of 5–10 nm, making them ideal for short gate lengths devices without the Schottky-gate instability observed for AlN HEMTs [10], [27], since the higher achievable barrier thickness and high dielectric constant reduce the susceptibility for Fowler–Nordheim tunneling. Reported data [2], [7], [9], [10], [12], [15], [16], [28] support the superior current density of AlScN HEMTs. When comparing the maximum drain current values with reported data of III-N HEMTs it can be derived, that even in the early stage of development AlScN-based HEMTs exhibit a high $I_{\mathrm{D,sat}}$ which could only be expected for AlGaN HEMTs with high Al content. However, when increasing the Al-content strain management becomes increasingly difficult which may cause poor OFF-state reliability [29] and is thus rather counterproductive to the increase in potential output power. Large variations of the drain current are assumed to be majorly caused by the large range of contact/access resistances reported ($R_C = 0.1$–$0.9\ \Omega\cdot$mm) and thus are the result of varying impact of extrinsic parasitics. Based on measured as well as reported results on n_s and υ_{EFF}, the measured saturation currents are significantly lower as theoretically predicted. Higher saturation currents have been reported but were either derived from open channel structures (3.3 A/mm) [12] or corresponding output curves (4.5 A/mm) were not shown above 1.5 A/mm [2]. Two major issues are assumed to cause this discrepancy.

1) Ohmic/access resistance is generally observed to be high for barrier materials with high Al fraction even for regrown n$^+$-GaN [2], [15], [16]. Large variations of the contact/access resistances have been reported so far (0.1–0.9 $\Omega\cdot$mm [2], [9], [15], [16]). Contact resistances of $R_C = 0.83$–$1.04\ \Omega\cdot$mm of the devices in this work were extracted by TLM.
2) The impact of process conditions is not well understood, which leaves the current maturity of the technology rather low compared to well-known AlGaN technology. Further improvement of the contact resistances, epitaxial growth, and process technology can be expected to allow for much higher current densities than reported so far [10].

D. Transconductance

In general, apart from drain conductance g_{ds} or output resistance r_{d}, transconductance g_m defines the possible intrinsic voltage gain ($A_V = g_m/g_{\mathrm{ds}} = g_m r_{\mathrm{D}}$) [23], [30] of a HEMT. Since the extrinsic g_m is affected by, e.g., access resistance the intr. transconductance $g_{m,i}$ is considered here to compare the barrier materials. The $g_{m,i}$ can be estimated in dependence of the material properties by the following equation [30]:

$$g_{m,i} = \frac{\varepsilon_0 \varepsilon_r}{\Delta d + d} \times \upsilon_{\mathrm{EFF}} \tag{3}$$

where ε_0, ε_r, Δd (1 nm [15]), d, and υ_{EFF} are the vacuum permittivity, the relative permittivity of the barrier, distance of the 2DEG centroid, barrier thickness, and the effective carrier velocity, respectively. Theoretically, for AlGaN-based devices, it is expected, that g_m decreases with increasing n_s [18] for a given barrier thickness as a result of reduced υ_{SAT} and larger C_{G} [30]. However, two major differences appear for AlScN: 1) AlScN provides a significantly larger n_s/t_{BAR}, which results in a lower $\upsilon_{\mathrm{EFF}}/t_{\mathrm{BAR}}$; and 2) AlScN is expected to have high-k dielectric properties significantly larger than AlGaN [3], [4]. Both effects exhibit a contrary impact on $g_{m,i}$. To account for the change in υ_{EFF} and ε_r, $g_{m,i}$ is calculated in dependence of the barrier thickness. The relative dielectric constants for the ternary material systems can be found in [1].

The effective carrier velocity is extrapolated using the n_s-dependence (for a given t_{BAR}) in the LOPE model described before. The calculated $g_{m,i}$ in dependence of the barrier thickness, as well as measured and reported data on the extrinsic g_m are given in Fig. 4. Even though reported AlScN-based HEMTs exhibit thicker barriers than AlN, the high ε_r enables similar $g_{m,i}$. When compared to common AlGaN-based heterostructures similar $g_{m,i}$ is obtained in the same range of t_{BAR}. However, it should be kept in mind, that the $I_{\mathrm{D,sat}}$ is more than three-times higher for AlScN-based devices. Experimental data of our devices were found to be lower ($g_m = 470$ and 490 mS/mm) as a result of the high contact resistance limiting the extrinsic $g_{m,\max}$. Reported data by other groups support the assumption of large $g_{m,\max}$ for barrier thicknesses in the range of 10 nm especially when considering the reported high contact resistances of AlScN HEMTs limiting the extrinsic g_m. This holds also true for AlN-based HEMTs, since the contact resistance scales more or less with the Al-content in the barrier. It can be concluded, that AlScN-based heterostructures provide significant advantages in terms of current density and transconductance when compared to common AlGaN-based HEMTs. Assuming a barrier thickness of 10 nm, AlScN HEMTs theoretically offer more than three-times the current density to AlGaN-based devices with Al content of around 30%. In addition, similar or slightly higher current gain can be expected both being beneficial in terms of output power. Moreover, the increase in achievable barrier thickness in combination with larger ε_r is expected to decrease tunneling transparency when compared to AlN- and AlGaN-based devices.

IV. OUTPUT POWER AND BANDWIDTH

Besides the power density (output power per gate periphery), the achievable matching bandwidth of devices is decisive for the exploitation of their full performance potential, in particular for applications that demand bandwidths of several gigahertz. This can be understood when examining the Bode–Fano limit [31], given for the output of a HEMT by the following equation:

$$\int_0^\infty \ln \frac{1}{|\Gamma(\omega)|} d\omega \leq \frac{\pi}{\tau_p}, \qquad \tau_p = R_{\mathrm{LL}} C_{\mathrm{out}} \tag{4}$$

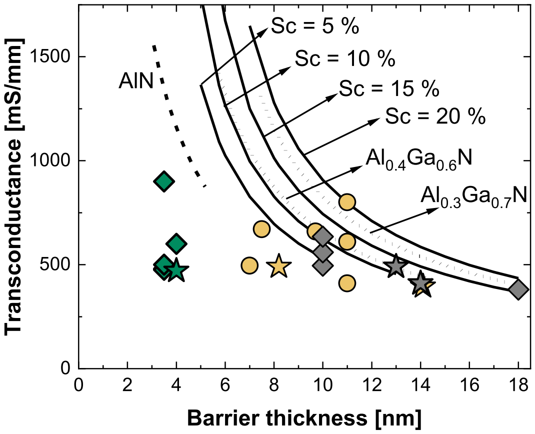

Fig. 4. Calculated intrinsic transconductance limits for AlN (dashed line), AlGaN (dotted line) and AlScN (straight lines). In addition, reported extrinsic transconductance data for AlN (green cubes), AlGaN (gray circles) and AlScN (yellow circles). Data obtained from this work are represented with stars with the same filling as reported data.

where $\Gamma(\omega)$, R_{LL}, and C_{out} are the frequency-dependent reflection coefficient, load-line resistance, and output capacitance of the transistor, respectively. Rearranging the expression according to [32] yields a simplified form of the Bode–Fano limit

$$\Delta f \leq -\frac{1}{2\tau_p \ln \Gamma_{\max}} = -\frac{1}{2 R_{\mathrm{LL}} C_{\mathrm{out}} \ln \Gamma_{\max}}. \tag{5}$$

Replacing R_{LL} with $R_{\mathrm{LL}} = 8P_{\mathrm{out}}/I_{\mathrm{D,sat}}^2$ yields

$$\Delta f \leq -\frac{I_{\mathrm{D,sat}}^2}{16 P_{\mathrm{out}} C_{\mathrm{out}} \ln \Gamma_{\max}}. \tag{6}$$

With P_{out} being the RF output power per gate periphery or power density. From (6) follows, that a higher Δf for a given device can only be achieved when lowering P_{out} and/or C_{out}. The latter is usually a function of device layout and the gate module, but cannot be designed independently. For devices employing a source-terminated field plate (STFP) C_{out} shows a dependency on n_s due to the coupling of the charge beneath the STFP with the STFP itself, manifesting as part of the drain–source capacitance (C_{ds}). Designing the STFP carefully or even eliminating it completely, reduces this portion of C_{ds} far enough so that it can be neglected. Based on this assumption we assume C_{ds} to be a technology-dependent constant for the following considerations. Hence, Δf can only be raised when lowering P_{out}, specifically by decreasing the supply voltage, which is contrary to the requirement of delivering high power. Therefore, it appears more logical to consider the product of P_{out} and Δf, which we call the power-bandwidth product (π_{PB}) given by the following equation:

$$\pi_{\mathrm{PB}} = \max(\Delta f \times P_{\mathrm{out}}) = -\frac{I_{\mathrm{D,sat}}^2}{16 C_{\mathrm{out}} \ln \Gamma_{\max}}. \tag{7}$$

Since, $\Gamma_{\max}$ is an (to some extend) arbitrarily chosen parameter, we can assign a constant value to it, e.g., −20 dB (or 0.1), a typical number for a power amplifier design [33]. The term $-\ln \Gamma_{\max}$ then becomes 2.3026. The power-bandwidth product

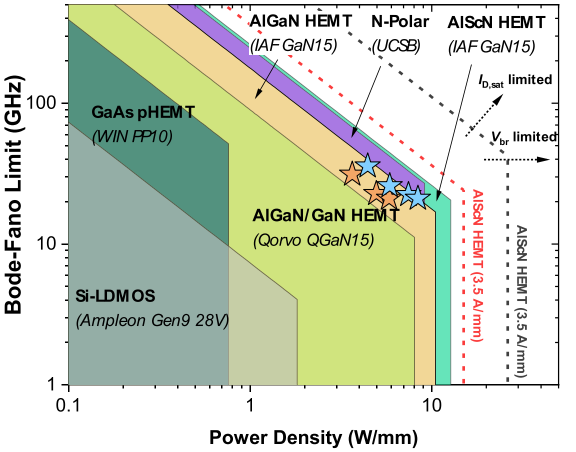

Fig. 5. Calculated intrinsic Bode–Fano limit versus power density for commercially available 28-V Si-LDMOS [33], 4-V GaAs pHEMT [34], 28-V AlGaN/GaN HEMTs [35], [36], 20-V N-polar GaN [21] as well as IAF's 30-V GaN15 for AlGaN/GaN and AlScN/GaN HEMTs along with experimental data of these (AlGaN/GaN: orange stars, AlScN/GaN: blue stars) [14]. The red and black dashed line shows the intrinsic theoretical limit for 30-V AlScN-HEMTs for and $I_{\mathrm{D,sat}}$ of 2 and 3.5 A/mm, respectively.

for this case simplifies to

$$\pi_{\mathrm{PB}} = \left.\frac{I_{\mathrm{D,sat}}^2}{36.8414 C_{\mathrm{out}}}\right|_{\Gamma_{\max}=-20\ \mathrm{dB}}. \tag{8}$$

The expression allows one to compare different technologies in terms of their intrinsic power-bandwidth product by knowing only two technology parameters. A graphical representation of the individual factors, P_{out} and Δf, for commercial Si-LDMOS [34], GaAs pHEMT [35], AlGaN/GaN [36], [37] HEMT as well as IAF's GaN15 AlGaN/GaN and AlScN/GaN HEMT technologies [9] is given in Fig. 5. It is clearly seen that the AlGaN/GaN HEMT not only features the highest power density of the commercially established technologies, but also a higher Bode–Fano limit than GaAs- or Si-based processes. Taking Qorvo's QGaN15 technology [36], [37] with a π_{PB} of 89.7 GHz Wmm^{-1}, we observe an improvement of more than a factor of two, when compared to WIN Semiconductors Corporation's PP10 GaAs pHEMT technology. Data of AlGaN/GaN and AlScN/GaN devices from [9], based on data of this work, show an even higher improvement factor of 3.1 and 4.5, respectively. Here, switching from an AlGaN to an AlScN barrier leads to a 1.45-times higher π_{PB} of 261.4 GHz Wmm^{-1}. This trend can be confirmed by comparing measurement data from the same devices, given in Fig. 5 by orange (AlGaN/GaN) and blue (AlScN/GaN) stars. The loads for maximum P_{out} at a V_{ds} of 15, 20, 25 V (AlGaN/GaN and AlScN/GaN) and additionally 30 V (AlScN) are shown. Similar to the intrinsic projection, a 1.45-times higher π_{PB} of 176.5 GHz Wmm^{-1} for the AlScN/GaN device is obtained. The absolute values of π_{PB} are roughly 33% smaller than the intrinsic limit, which can be attributed to extrinsic parasitic effects, e.g., nonzero ON-resistance and charge trapping [9]. Roughly similar values are obtained for N-polar devices [38] (since the sheet carrier density is roughly equivalent) which display the limit of high Al-content (38%) devices. In order to assess the theoretical intrinsic limit of reported AlScN/GaN HEMTs we assume an identical C_{out} as for our AlGaN devices but an $I_{\mathrm{D,sat}}$ of 2 A/mm, which is consistent with recent publications of demonstrated devices [9], [12], [15], [39]. The projected π_{PB} is around 9.5-times higher than that obtained by WIN's PP10. Benchmarking it against Qorvo's QGaN15 and the devices of this work with the AlGaN barrier, the calculated π_{PB} is still higher by a factor of four and two, respectively. As given in Fig. 3, even higher values of $I_{\mathrm{D,sat}}$ for the AlScN-based devices are theoretically possible, but have not been demonstrated yet. For completeness, Fig. 5 also shows the intrinsic limit for an $I_{\mathrm{D,sat}}$ of 3.5 A/mm. Although the power-bandwidth product allows to quantify a technology's capability to simultaneously deliver high power and wide-bandwidth matching capability, it does not consider its high-frequency properties. The latter can be included by multiplying the power-bandwidth product with the transition frequency f_T, which is given by the following equation:

$$f_T = \frac{g_{m,i}}{2\pi C_g} = \frac{v_{\mathrm{SAT}}}{2\pi l_g}. \tag{9}$$

With $g_{m,I}$, l_g, and C_g being the intrinsic transconductance, gate capacitance of a Schottky junction and the device gate length. By multiplying f_T with the power-bandwidth product, we obtain the power-bandwidth-transition-frequency product (π_{PBT})

$$\pi_{\mathrm{PBT}} = -\frac{(en_s)^2 v_{\mathrm{SAT}}^3}{32\pi C_{\mathrm{out}} l_g \ln \Gamma_{\max}}. \tag{10}$$

Replacing v_{SAT} with (2) yields

$$\pi_{\mathrm{PBT}} = -\frac{10^{21}(en_s)^2}{32\pi C_{\mathrm{out}} l_g \ln \Gamma_{\max}\left(0.38 + \left(\frac{n_s}{n_{s,0}}\right)^{0.45}\right)^3}. \tag{11}$$

We can express the following proportionality for an n_s from 1×10^{13} to $4 \times 10^{13}\ \mathrm{cm}^{-2}$:

$$\pi_{\mathrm{PBT}} \propto \frac{n_s^2}{\left(0.38 + \left(\frac{n_s}{n_{s,0}}\right)^{0.45}\right)^3} \approx \frac{n_s}{1.5 \times 10^{-13}} \propto n_s. \tag{12}$$

It is rather striking to see, that this figure of merit reduces to a single dependent variable despite the large number of terms to start with. Although n_s can effectively be considered a technology-dependent variable, it is not limited by the technology itself, but by the employed barrier material and its respective stoichiometry, as can be seen in Fig. 1. We can, therefore, conclude that for an n_s from 1×10^{13} to $4 \times 10^{13}\ \mathrm{cm}^{-2}$, π_{PBT} describes the same trend as n_s itself. This finding, ultimately, highlights the enormous potential of AlScN HEMTs as wideband high-power mm-wave devices.

V. CONCLUSION

In this work, the theoretical limits of AlScN-based HEMTs are estimated in terms of saturation current, transconductance, output power, and bandwidth. Time delays are extracted and corresponding high-field carrier velocities are reported for the first time. Based on the transport properties the achievable current density and transconductance are described in dependence of the barrier thickness. In addition, the output power and matching bandwidth are derived demonstrating the superior capability of AlScN/GaN HEMTs for combining high bandwidth, output power, and frequency. An increase of 1.45-times the power-bandwidth product is demonstrated for AlScN-based HEMTs compared to conventional AlGaN/GaN HEMTs further highlighting its potential as wideband, high-power mm-wave devices.

REFERENCES

[1] O. Ambacher, B. Christian, M. Yassine, M. Baeumler, S. Leone, and R. Quay, "Polarization induced interface and electron sheet charges of pseudomorphic ScAlN/GaN, GaAlN/GaN, InAlN/GaN, and InAlN/InN heterostructures," *J. Appl. Phys.*, vol. 129, no. 20, May 2021, Art. no. 204501, doi: 10.1063/5.0049185.

[2] J. Casamento et al., "FerroHEMTs: High-current and high-speed all-epitaxial AlScN/GaN ferroelectric transistors," in *IEDM Tech. Dig.*, San Francisco, CA, USA, Dec. 2022, pp. 11.1.1–11.1.4.

[3] J. Casamento et al., "Epitaxial $Sc_xAl_{1-x}N$ on GaN exhibits attractive high-K dielectric properties," *Appl. Phys. Lett.*, vol. 120, no. 15, Apr. 2022, Art. no. 152901, doi: 10.1063/5.0075636.

[4] O. Ambacher et al., "Wurtzite ScAlN, InAlN, and GaAlN crystals, a comparison of structural, elastic, dielectric, and piezoelectric properties," *J. Appl. Phys.*, vol. 130, no. 4, Jul. 2021, Art. no. 045102, doi: 10.1063/5.0048647.

[5] O. Ambacher, A. Yassine, M. Yassine, S. Mihalic, E. Wade, and B. Christian, "Electron accumulation and distribution at interfaces of hexagonal $Sc_xAl_{1-x}N$/GaN- and $Sc_xAl_{1-x}N$/InN-heterostructures," *J. Appl. Phys.*, vol. 131, no. 24, Jun. 2022, Art. no. 245702, doi: 10.1063/5.0094533.

[6] J. Ligl et al., "Metalorganic chemical vapor phase deposition of AlScN/GaN heterostructures," *J. Appl. Phys.*, vol. 127, no. 19, May 2020, Art. no. 195704, doi: 10.1063/5.0003095.

[7] C. Manz et al., "Improved AlScN/GaN heterostructures grown by metal-organic chemical vapor deposition," *Semicond. Sci. Technol.*, vol. 36, no. 3, Mar. 2021, Art. no. 034003, doi: 10.1088/1361-6641/abd924.

[8] I. Streicher et al., "Effect of AlN and AlGaN interlayers on AlScN/GaN heterostructures grown by metal–organic chemical vapor deposition," *Crystal Growth Des.*, vol. 23, no. 2, pp. 782–791, Feb. 2023, doi: 10.1021/acs.cgd.2c01013.

[9] S. Krause, I. Streicher, P. Waltereit, L. Kirste, P. Brückner, and S. Leone, "AlScN/GaN HEMTs grown by metal–organic chemical vapor deposition with 8.4 W/mm output power and 48% power-added efficiency at 30 GHz," *IEEE Electron Device Lett.*, vol. 44, no. 1, pp. 17–20, Jan. 2023, doi: 10.1109/LED.2022.3220877.

[10] P. Döring et al., "Voltage-margin limiting mechanisms of AlScN-based HEMTs," *Appl. Phys. Lett.*, vol. 123, no. 3, Jul. 2023, Art. no. 032101, doi: 10.1063/5.0159501.

[11] B. K. Ridley, "Polarization-induced electron populations," *Appl. Phys. Lett.*, vol. 77, no. 7, pp. 990–992, Aug. 2000, doi: 10.1063/1.1288817.

[12] T. E. Kazior, E. M. Chumbes, B. Schultz, J. Logan, D. J. Meyer, and M. T. Hardy, "High power density ScAlN-based heterostructure FETs for mm-wave applications," in *IEEE MTT-S Int. Microw. Symp. Dig.*, Boston, MA, USA, Jun. 2019, pp. 1136–1139.

[13] P. Wang et al., "Quaternary alloy ScAlGaN: A promising strategy to improve the quality of ScAlN," *Appl. Phys. Lett.*, vol. 120, no. 1, Jan. 2022, Art. no. 012104, doi: 10.1063/5.0060608.

[14] E. N. Jin et al., "Impact of surface preparation on the epitaxial growth of $SrTiO_3$ on ScAlN/GaN heterostructures," *J. Appl. Phys.*, vol. 134, no. 2, Jul. 2023, Art. no. 025303, doi: 10.1063/5.0152694.

[15] A. J. Green et al., "RF power performance of Sc(Al,Ga)N/GaN HEMTs at Ka-band," *IEEE Electron Device Lett.*, vol. 41, no. 8, pp. 1181–1184, Aug. 2020, doi: 10.1109/LED.2020.3006035.

[16] A. J. Green et al., "ScAlN/GaN high-electron-mobility transistors with 2.4-A/mm current density and 0.67-S/mm transconductance," *IEEE Electron Device Lett.*, vol. 40, no. 7, pp. 1056–1059, Jul. 2019, doi: 10.1109/LED.2019.2915555.

[17] S. Bajaj et al., "Density-dependent electron transport and precise modeling of GaN high electron mobility transistors," *Appl. Phys. Lett.*, vol. 107, no. 15, Oct. 2015, Art. no. 153504, doi: 10.1063/1.4933181.

[18] T. Fang, R. Wang, H. Xing, S. Rajan, and D. Jena, "Effect of optical phonon scattering on the performance of GaN transistors," *IEEE Electron Device Lett.*, vol. 33, no. 5, pp. 709–711, May 2012, doi: 10.1109/LED.2012.2187169.

[19] J. M. Barker, D. K. Ferry, D. D. Koleske, and R. J. Shul, "Bulk GaN and AlGaN/GaN heterostructure drift velocity measurements and comparison to theoretical models," *J. Appl. Phys.*, vol. 97, no. 6, Mar. 2005, Art. no. 063705, doi: 10.1063/1.1854724.

[20] N. Moll, M. R. Hueschen, and A. Fischer-Colbrie, "Pulse-doped AlGaAs/InGaAs pseudomorphic MODFETs," *IEEE Trans. Electron Devices*, vol. 35, no. 7, pp. 879–886, Jul. 1988, doi: 10.1109/16.3339.

[21] B. Romanczyk et al., "Bias-dependent electron velocity extracted from N-polar GaN deep recess HEMTs," *IEEE Trans. Electron Devices*, vol. 67, no. 4, pp. 1542–1546, Apr. 2020, doi: 10.1109/TED.2020.2973081.

[22] P. T. Coleridge, "Inter-subband scattering in a 2D electron gas," *Semicond. Sci. Technol.*, vol. 5, no. 9, pp. 961–966, Sep. 1990, doi: 10.1088/0268-1242/5/9/006.

[23] K. Shinohara et al., "220 GHz f_T and 400 GHz f_{max} in 40-nm GaN DH-HEMTs with re-grown ohmic," in *IEDM Tech. Dig.*, San Francisco, CA, USA, Dec. 2010, pp. 30.1.1–30.1.4.

[24] A. Agboton et al., "Electron delay analysis and image charge effect in AlGaN/GaN HEMT on silicon substrate," in *Proc. Eur. Solid-State Device Res. Conf. (ESSDERC)*, Bucharest, Romania, Sep. 2013, pp. 57–60.

[25] Y. Yue et al., "InAlN/AlN/GaN HEMTs with regrown ohmic contacts and f_T of 370 GHz," *IEEE Electron Device Lett.*, vol. 33, no. 7, pp. 988–990, Jul. 2012, doi: 10.1109/LED.2012.2196751.

[26] M. Higashiwaki, T. Mimura, and T. Matsui, "AlN/GaN insulated-gate HFETs using cat-CVD SiN," *IEEE Electron Device Lett.*, vol. 27, no. 9, pp. 719–721, Sep. 2006, doi: 10.1109/led.2006.881087.

[27] K. D. Chabak et al., "High-performance AlN/GaN HEMTs on sapphire substrate with an oxidized gate insulator," *IEEE Electron Device Lett.*, vol. 32, no. 12, pp. 1677–1679, Dec. 2011, doi: 10.1109/LED.2011.2167952.

[28] M. B. Tahhan et al., "Passivation schemes for ScAlN-barrier mm-wave high electron mobility transistors," *IEEE Trans. Electron Devices*, vol. 69, no. 3, pp. 962–967, Mar. 2022, doi: 10.1109/TED.2021.3140016.

[29] J. Joh and J. A. del Alamo, "Mechanisms for electrical degradation of GaN high-electron mobility transistors," in *IEDM Tech. Dig.*, San Francisco, CA, USA, Mar. 2006, pp. 1–4.

[30] U. K. Mishra and J. Singh, *Semiconductor Device Physics and Design*. Dordrecht, The Netherlands: Springer, 2007.

[31] R. M. Fano, "Theoretical limitations on the broadband matching of arbitrary impedances," *J. Franklin Inst.*, vol. 249, no. 1, pp. 57–83, Jan. 1950.

[32] F. Sechi, *Solid-State Microwave High-Power Amplifiers*, 1st ed. Norwood, MA, USA: Artech House, 2009. [Online]. Available: https://ebookcentral.proquest.com/lib/kxp/detail.action?docID=946555

[33] P. Neininger et al., "Limitations and implementation strategies of interstage matching in a 6-W, 28–38-GHz GaN power amplifier MMIC," *IEEE Trans. Microw. Theory Techn.*, vol. 69, no. 5, pp. 2541–2553, May 2021, doi: 10.1109/TMTT.2021.3065108.

[34] S. J. C. H. Theeuwen, H. Mollee, R. Heeres, and F. Van Rijs, "LDMOS technology for power amplifiers up to 12 GHz," in *Proc. 13th Eur. Microw. Integr. Circuits Conf. (EuMIC)*, Sep. 2018, pp. 162–165.

[35] H.-T. Lin, C.-H. Chen, S.-C. Lee, and I.-T. Cho, *6 Inch 0.1μm GaAs pHEMT Technology for E/V Band Application*, Palm Springs, CA, USA: CS ManTech, 2011.

[36] S. Nayak et al., *0.15μm GaN MMIC Manufacturing Technology for 2–50 GHz Power Applications*. Scttsdale, AZ, USA: CS ManTech, 2015.

[37] C. F. Campbell, Y. Liu, M.-Y. Kao, and S. Nayak, "High efficiency Ka-band gallium nitride power amplifier MMICs," in *Proc. IEEE Int. Conf. Microw., Commun., Antennas Electron. Syst. (COMCAS)*, Oct. 2013, pp. 1–5.

[38] B. Romanczyk et al., "Demonstration of constant 8 W/mm power density at 10, 30, and 94 GHz in state-of-the-art millimeter-wave N-polar GaN MISHEMTs," *IEEE Trans. Electron Devices*, vol. 65, no. 1, pp. 45–50, Jan. 2018, doi: 10.1109/TED.2017.2770087.

[39] E. M. Chumbes et al., "ScAlN-GaN transistor technology for millimeter-wave ultra-high power and efficient MMICs," in *IEEE MTT-S Int. Microw. Symp. Dig.*, Denver, CO, USA, Jun. 2022, pp. 295–297.